JⱮ PAPERS

Effects of oscillating gas-phase flow on an evaporating multicomponent droplet

Sreeparna Majee[1]**, Abhishek Saha**[2,†]** and Saptarshi Basu**[1,†]

[1]Department of Mechanical Engineering, Indian Institute of Science, Bengaluru, Karnataka 560012, India

[2]Department of Mechanical and Aerospace Engineering, University of California San Diego, La Jolla, CA 92093, USA

The dynamics of an evaporating droplet in an unsteady flow is of practical interest in many industrial applications and natural processes. To investigate the transport and evaporation dynamics of such droplets, we present a numerical study of an isolated droplet in an oscillating gas-phase flow. The study uses a one-way coupled two-phase flow model to assess the effect of the amplitude and the frequency of a sinusoidal external flow field on the lifetime of a multicomponent droplet containing a non-volatile solute dissolved in a volatile solvent. The results show that the evaporation process becomes faster with an increase in the amplitude or the frequency of the gas-phase oscillation. The liquid-phase transport inside the droplet also is influenced by the unsteadiness of the external gas-phase flow. A scaling analysis based on the response of the droplet under the oscillating drag force is subsequently carried out to unify the observed evaporation dynamics in the simulations under various conditions. The analysis quantifies the enhancement in the droplet velocity and Reynolds number as a function of the gas-phase oscillation parameters and predicts the effects on the evaporation rate.

1. Introduction

Heat and mass transfers in droplets moving in an unsteady flow are ubiquitous in both engineering and geophysical systems. For example, fuel droplets are sprayed in an unsteady turbulent flow in internal combustion engines, gas turbines and liquid-fuelled rocket engines (Mellor 1980; Law 1982; Birouk & Gokalp 2006; Cantwell, Karabeyoglu & Altman 2010; Perini & Reitz 2016). The unsteady dynamics of evaporation of the

† Email addresses for correspondence: asaha@eng.ucsd.edu; sbasu@iisc.ac.in

droplets and transport of the fuel vapour critically affect the subsequent combustion processes and, thus, power or thrust generation and ensuing emissions. Interaction between unsteady flow and evaporating droplets is also present in thermal sprays, where the injected droplets carrying functional materials undergo evaporation, precipitation and chemical transformation in either a turbulent plasma (solution precursor plasma process) (Pawlowski 2009; Jordan, Jiang & Gell 2015) or a high-velocity oxy-fuel flame environment (Basu & Cetegen 2008; Li & Christofides 2009). Irrespective of the method, the quality of the coating generated with thermal sprays depends on the evaporation dynamics and droplet lifetime (Basu, Jordan & Cetegen 2008; Saha *et al.* 2009*a*; Saha, Kumar & Basu 2010).

Among geophysical systems, the unsteady flow in the upper atmosphere has a strong influence on the formation of raindrops and clouds. Atmospheric turbulence, indeed, is critical in accumulating or dispersing particles that serve as nucleation sites for water vapour to condense and form clouds and raindrops (Shaw *et al.* 1998; Vaillancourt & Yau 2000; Shaw 2003; Ruehl, Chuang & Nenes 2008; Grabowski & Wang 2013).

Recently, droplet evaporation and transport in an unsteady flow have gained great interest due to their direct relation to the transmission of COVID-19, a disease whose virus primarily transmits through respiratory droplets. Studies have been performed to account for the unsteady turbulent jet and puff emanating from oral and nasal cavities along with the respiratory droplets (Balachandar *et al.* 2020; Chaudhuri *et al.* 2020*a*; Jayaweera *et al.* 2020; Mittal, Ni & Seo 2020; World Health Organization 2020; Bourouiba 2021), to understand their effect on evaporation patterns (Basu *et al.* 2020; Bourouiba 2020; Chaudhuri *et al.* 2020*a*; Rosti *et al.* 2021; Saha *et al.* 2022) and build disease transmission models (Chaudhuri, Basu & Saha 2020*b*). Simultaneously, several studies have focused on the unsteady dynamics of ambient airflow and their influence on the transport of respiratory droplets (Dbouk & Drikakis 2020; Chong *et al.* 2021; Ng *et al.* 2021; Sharma *et al.* 2022). For example, Chong *et al.* (2021) and Ng *et al.* (2021) have shown that the unsteadiness in local flow patterns and humidity can lead to growth and clustering among the dispersed respiratory droplets. Other studies (Bhagat *et al.* 2020; Somsen *et al.* 2020) have investigated how spatial and temporal variation in indoor air can influence the transport of these respiratory droplets and, hence, the transmission of the disease.

The above review of the literature demonstrates that droplet evaporation in unsteady conditions is, indeed, of interest to various engineering, atmospheric and health problems. Naturally, the fundamental aspects of droplet evaporation have received attention in the thermal fluids community. Droplet evaporation in a steady or weakly unsteady environment has been extensively studied in a wide range of situations and configurations, using both theory, experiment and simulation. These studies have paved the way to a detailed understanding of the topic, which has been summarized periodically in review articles (Law 1982; Sirignano 1983; Aggarwal & Peng 1995; Sazhin 2006, 2017; Saha, Deepu & Basu 2018).

Droplet evaporation in an unsteady flow field has also received attention from the research community. The interaction between a vortex and a droplet with comparable length scales has been studied by Kim, Elghobashi & Sirignano (1995), where they investigated the variations in the droplet drag coefficient due to the droplet–vortex interplay. Masoudi & Sirignano (2000) investigated the influence of droplet–vortex collision on the simultaneous heating, evaporation and mass transfer of the droplet. The interaction of evaporating droplets with a Kármán vortex sheet was studied by

Burger *et al.* (2006) to predict a complex vapour–air mixing process. Fundamental studies with particle dispersion and phase interaction in large vortex structures have also been addressed by researchers (Lazaro & Lasheras 1992; Tang *et al.* 1992; Aggarwal, Park & Katta 1996; Marcu & Meiburg 1996; Harstad & Bellan 1997; Kim, Elghobashi & Sirignano 1997). It was shown that the dynamics of vortex structures typically governs the mass and momentum exchanges of the droplet dynamics (Clemens & Mungal 1995). Moreover, the dispersion of spray droplets is highly dependent on the surrounding vortex dynamics, and local shearing vortices tend to govern the response behaviour of the droplets (Reveillon & Vervisch 2005).

While the above studies have illustrated droplet dynamics in a complex unsteady non-uniform vortical flow field, they were mostly performed for droplets containing pure liquid. However, in many applications, the droplet liquid contains non-volatile dissolved components. In this work, we describe a framework to study the evaporation dynamics of an isolated binary droplet (containing solvent and solute) in a simpler unsteady oscillating flow field. The primary goal is to identify the response in droplet evaporation rate and the underlying mechanistic description for such a response. Finally, we will show similarity and dissimilarity among the responses under various unsteady conditions using proper non-dimensional time scales. We will accomplish these goals by formulating a two-dimensional numerical model for binary droplets, assuming one-way coupling between the droplet and the periodic perturbation in gas-phase velocity. This model, which was originally developed by Abramzon & Sirignano (1989), provides a complete analysis with a detailed numerical simulation for the liquid phase coupled with the gas phase governing the droplet dynamics moving in the air. We have imposed an unsteady gas-phase flow condition to simulate the oscillating flow. The cornerstone of this article is the development of a theoretical relation between gas-phase frequency and the droplet velocity responsible for the modified evaporation of the oscillating droplet motion.

2. Mathematical modelling

The motion of any droplet moving in unsteady flow can be described by the drag force experienced by the droplet due to its relative velocity with respect to the surrounding gas phase. The transport of these droplets depends on the perturbation characteristics of the unsteadiness that interacts periodically with the droplets. Moreover, the evaporation of any binary fluid is an intricate process due to the complex heat and mass transfer in the gas phase and liquid phase, where the latter is affected by the spatial distribution of the non-volatile solute and solvent concentration. The two-dimensional model used in this work uses a detailed description of liquid-phase transport, which on many occasions is ignored due to computational complexities. The mathematical modelling framework herein is adapted from Abramzon & Sirignano (1989) for the evaporation of a moving droplet, extending the classical droplet evaporation model under the influence of Stefan flow (blowing) on heat and mass transfer and the effect of internal circulation in the liquid phase of the droplet. We will, next, describe the model and its governing equations.

First, we look into the global transport of the droplet by solving the drag equation. The complete descriptions of the drag equations are given below:

$$\frac{\mathrm{d}U_p}{\mathrm{d}t} = \frac{3C_D}{8r_s}\left(\frac{\rho_g}{\rho_l}\right)|U_g - U_p|(U_g - U_p), \tag{2.1}$$

956 A17-3

$$\frac{\mathrm{d}X_p}{\mathrm{d}t} = U_p, \tag{2.2}$$

$$\frac{\mathrm{d}V_p}{\mathrm{d}t} = \frac{3C_D}{8r_s}\left(\frac{\rho_g}{\rho_l}\right)|V_g - V_p|(V_g - V_p) + \frac{(\rho_l - \rho_g)}{\rho_l}g, \tag{2.3}$$

$$\frac{\mathrm{d}Y_p}{\mathrm{d}t} = V_p. \tag{2.4}$$

Here X_p (or Y_p) and U_p (or V_p) are the horizontal (or vertical) displacement and instantaneous velocity of the droplet, respectively; t is time; U_g and V_g are the gas-phase velocities in the horizontal and vertical directions, respectively; C_D is the drag coefficient; ρ_g and ρ_l are the densities of the gas phase and liquid phase, respectively; and r_s is the instantaneous radius of the droplet. The body force is accounted for generally using g, the gravitational acceleration. The liquid-phase density is calculated based on the mass fractions of the components. Since the overall solute concentration changes with time due to evaporation, ρ_l is not constant with time.

Since we are interested in capturing the unsteady perturbation of one dimension of the gas-phase flow, we have assumed vertical gas-phase flow is weak ($V_g = 0$) and have neglected the body force term (so $g = 0$). The drag forces from the added-mass effects and Basset history force (Odar & Hamilton 1964; Berlemont, Desjonqueres & Gouesbet 1990) for our simulation conditions are relatively weak, and hence we have neglected their contributions. See the supplementary material available at https://doi.org/10.1017/jfm.2023.30 for the details. The simplified drag equation above can then be linearized for Stokes flow conditions by setting the drag coefficient, $C_D = 24/Re_p$, where the gas-phase Reynolds number is defined as

$$Re_p = 2\rho_g|U_g - U_p|r_s/\mu_g, \tag{2.5}$$

where μ_g is the gas-phase dynamic viscosity.

Under these conditions, the droplet motion is described by

$$\frac{\mathrm{d}U_p}{\mathrm{d}t} = \frac{9}{2\tau}(U_g - U_p), \quad \tau = \frac{\rho_l r_s^2}{\mu_g}, \tag{2.6}$$

where τ is the droplet response time. Now, to assess the response of the isolated droplet exposed to an oscillating gas flow field, the gas velocity U_g in (2.6) is assumed to have a sinusoidal perturbation,

$$U_g = U_{g,0} + a\sin(\omega t), \tag{2.7}$$

where $U_{g,0}$ is the mean gas-phase velocity, a is the amplitude and $\omega (= 2\pi f)$ is the angular frequency, with f being the frequency of oscillation in the gas-phase velocity.

Next, we describe the mass and heat transfer parts of the model. The change in droplet radius due to evaporation is defined as

$$\frac{\mathrm{d}r_s}{\mathrm{d}t} = -\frac{\dot{m}}{4\pi\rho_l r_s^2}, \tag{2.8}$$

where $\dot{m}$ is the rate of change of the droplet's liquid mass due to evaporation. In the vapour phase during droplet evaporation, the average temperature is defined to be $T_{mean} = (2T_s + T_\infty)/3$ as suggested by Hubbard, Denny & Mills (1975), where T_s and T_∞ are, respectively, the droplet surface temperature and temperature of the gas phase. By assuming the vapour

phase surrounding the liquid droplet as a quasi-steady-state condition, the expressions for evaporation mass flux (mass and heat transfer limits) are given as

$$\dot{m} = 2\pi \rho_v D_v r_s Sh^* \log(1 + B_M) \qquad (2.9)$$

and

$$\dot{m} = 2\pi \rho_v \alpha_g r_s Nu^* \log(1 + B_T), \qquad (2.10)$$

where $\dot{m}$ is as given above, ρ_v is the density of water vapour, D_v is the binary diffusivity of liquid vapour in the gas phase, α_g is the thermal diffusivity of the surrounding gas phase, and the modified Sherwood and Nusselt numbers are defined below. In the above, $B_M = (Y_{w,s} - Y_{w,\infty})/(1 - Y_{w,s})$ and $B_T = C_{p,l}(T_\infty - T_s)/(h_{fg} - \dot{Q}_l/\dot{m})$ are the Spalding mass and heat transfer numbers. Here, $Y_{w,s}$ and $Y_{w,\infty}$ are the liquid vapour fractions at the droplet surface and far field, respectively; $C_{p,l}$ and $h_{f,g}$ are the specific heat of the droplet and latent heat for evaporation of the solvent in the droplet; and $\dot{Q}_l$ is the amount of heat transferred to or from the droplet. Further details can be found in (Abramzon & Sirignano 1989) and Majee *et al.* (2021).

In (2.9) and (2.10), Nu^* and Sh^* are the modified Nusselt and Sherwood numbers. Using the quasi-steady assumption, the Nusselt and Sherwood numbers for a non-evaporating sphere can be defined as (Clift, Grace & Weber 2005)

$$Nu_0 = 1 + (1 + Re_p Pr)^{1/3} f(Re) \qquad (2.11)$$

and

$$Sh_0 = 1 + (1 + Re_p Sc)^{1/3} f(Re), \qquad (2.12)$$

where $Pr\ (= \mu_g/(\alpha_g \rho_g))$ and $Sc\ (= \mu_g/(D_v \rho_g))$ are Prandlt and Schmidt numbers, respectively; and $f(Re)$ is the correction factor for the Reynolds number effect, the correction being

$$f(Re_p) = 1, \quad Re_p \leq 1, \qquad (2.13)$$

$$f(Re_p) = Re_p^{0.077}, \quad 1 < Re_p \leq 400. \qquad (2.14)$$

Two physical effects distinguish the heat and mass transfer in evaporating droplets from those of steady-state non-evaporating spheres. First, the surface-blowing effect due to evaporation changes the boundary layer. Furthermore, there exists an asymmetry in the boundary layer along the droplet interface at various angular locations that causes an asymmetry in local heat and mass transfer. Abramzon & Sirignano (1989) accounted for these effects by correcting the Nusselt and Sherwood numbers and, thereby, the global heat and mass transfer rates. The corrected Nusselt and Sherwood numbers, Nu^* and Sh^*, can be expressed as

$$Nu^* = 2 + \frac{Nu_0 - 2}{F(B_T)} \qquad (2.15)$$

and

$$Sh^* = 2 + \frac{Sh_0 - 2}{F(B_M)}, \qquad (2.16)$$

where $F(B) = (1 + B)^{0.7}(\ln(1 + B))/B$. Further details are provided in Abramzon & Sirignano (1989) and Sirignano (2010).

In a binary droplet, the non-volatile component suppresses the vapour pressure of the volatile component at the droplet surface. This phenomenon is taken into account by considering an ideal solution that obeys Raoult's law (Van Wylen & Sonntag 1978), $P_{vap}(T_s, \chi_{w,s}) = \chi_{w,s}P_{sat}(T_s)$, where $\chi_{w,s}$ is the mole fraction of volatile solvent at the droplet surface in the liquid phase. We note that, for non-ideal solutions, the vapour pressure of the evaporating species at the droplet surface can be evaluated by considering the activity coefficients of each species in the mixture, as discussed in several studies (Senda *et al.* 2000; Bader, Keller & Hasse 2013; Chen *et al.* 2016; Borodulin, Nizovtsev & Sterlyagov 2019; Fang *et al.* 2019).

After having considered the mass evaporation rate of the droplet, we will now look into the liquid phase to understand the spatio-temporal temperature and concentration distributions of the evaporating droplet. In this work, any possible deformation in droplet shape due to aerodynamic forces has been neglected. This can be justified by assessing the gas-phase Weber number, $We = 2\rho_g(|U_p - U_g|)^2 r_s/\sigma$, which is significantly less than 1 for the conditions of this study. The liquid phase of a spherical droplet translating in the gas phase experiences convective vortical motion due to relative velocity and, thus, shear stress at the liquid–gas interface. Abramzon & Sirignano (1989) showed, for such droplets, that the internal flow structure can be modelled as the well-known two-dimensional Hill's spherical vortex (Lamb 1993). The explicit solution for a Hill's spherical vortex renders expressions for the radial and angular velocities in the spherical coordinate system (r, θ) in the liquid phase as follows:

$$V_r = -U_s \left(1 - \frac{r^2}{r_s^2}\right) \cos \theta, \tag{2.17}$$

and

$$V_\theta = U_s \left(1 - 2\frac{r^2}{r_s^2}\right) \sin \theta. \tag{2.18}$$

Here $U_s = (1/32)(U_g - U_p)(\mu_g/\mu_l)Re_pC_F$ is the liquid velocity at the vapour–liquid interface and is calculated by the continuity of the shear stress across the interface; μ_l is the liquid-phase dynamic viscosity; and C_F is the skin friction coefficient for an evaporating sphere calculated using the correlation given by Renksizbulut & Yuen (1983) as

$$C_F = \frac{12.69Re_p^{-2/3}}{1 + B_M}. \tag{2.19}$$

It is to be noted that thermal and concentration gradients across the droplet interface can induce Marangoni stress, which can be important for modelling the evaporation of multicomponent droplets (Niazmand *et al.* 1994; Dwyer *et al.* 1996; Dwyer, Shaw & Niazmand 1998). However, for the present study, the gradients are small, and, as such, the Marangoni flow velocity is expected to be smaller than the shear-driven flow (U_s) at the droplet surface. A detailed comparison is shown in the supplementary material.

The non-dimensional conservation equations of energy and mass fraction in the liquid phase are given by (Ozturk & Cetegen 2004)

$$\overline{r_s^2}\frac{\partial \bar{T}}{\partial \bar{t}} + (0.5Pe_l\overline{V_r}\overline{r_s} - \beta\eta)\frac{\partial \bar{T}}{\partial \eta} + 0.5Pe_l\frac{\overline{V_\theta}\overline{r_s}}{\eta}\frac{\partial \bar{T}}{\partial \theta}$$

$$= \frac{1}{\eta^2}\frac{\partial}{\partial \eta}\left(\eta^2\frac{\partial \bar{T}}{\partial \eta}\right) + \frac{1}{\eta^2 \sin \theta}\frac{\partial}{\partial \theta}\left(\sin \theta\frac{\partial \bar{T}}{\partial \theta}\right) \tag{2.20}$$

and

$$Le_l \overline{r_s^2} \frac{\partial \overline{Y_N}}{\partial \bar{t}} + (0.5 Pe_l Le_l \overline{V_r} \overline{r_s} - Le_l \beta \eta) \frac{\partial \overline{Y_N}}{\partial \eta} + 0.5 Pe_l Le_l \frac{\overline{V_\theta} \overline{r_s}}{\eta} \frac{\partial \overline{Y_N}}{\partial \theta}$$

$$= \frac{1}{\eta^2} \frac{\partial}{\partial \eta} \left(\eta^2 \frac{\partial \overline{Y_N}}{\partial \eta} \right) + \frac{1}{\eta^2 \sin \theta} \frac{\partial}{\partial \theta} \left(\sin \theta \frac{\partial \overline{Y_N}}{\partial \theta} \right), \tag{2.21}$$

respectively. Equations (2.20) and (2.21) are solved using the initial and boundary conditions,

$$\bar{t} = 0 \rightarrow \bar{T} = 0,$$

$$\left. \begin{array}{l} \eta = 1, \quad \begin{cases} \dfrac{\partial \bar{T}}{\partial \theta} = 0, \\ \displaystyle\int_0^\pi \dfrac{\partial \bar{T}}{\partial \eta} \sin \theta \, \mathrm{d}\theta = \dfrac{\dot{Q}_l}{2\pi r_s k_l T_0}, \end{cases} \\[20pt] \theta = 0, \quad \pi \rightarrow \dfrac{\partial \bar{T}}{\partial \theta} = 0, \end{array} \right\} \tag{2.22}$$

and

$$\bar{t} = 0 \rightarrow \overline{Y_N} = 0,$$

$$\left. \begin{array}{l} \eta = 1, \quad \begin{cases} \dfrac{\partial \overline{Y_N}}{\partial \theta} = 0, \\ \displaystyle\int_0^\pi \dfrac{\partial \overline{Y_N}}{\partial \eta} \sin \theta \, \mathrm{d}\theta = \dfrac{\dot{m}}{2\pi \rho_l r_s D_{v,za} Y_{N,0}}, \end{cases} \\[20pt] \theta = 0, \quad \pi \rightarrow \dfrac{\partial \overline{Y_N}}{\partial \theta} = 0, \end{array} \right\} \tag{2.23}$$

respectively. Here, $\overline{r_s} = r_s/r_0$ is the non-dimensional droplet radius; $\eta = r/r_s$ is the non-dimensional radial coordinate; $\overline{V_r} = V_r/U_s$ and $\overline{V_\theta} = V_\theta/U_s$ are the non-dimensional velocities (radial and angular, respectively); $\bar{T} = (T - T_0)/T_0$ is the non-dimensional temperature; $\bar{t} = \alpha_l t/r_0^2$ is the non-dimensional time; $\beta = 0.5 \partial \overline{r_s}/\partial \bar{t}$ is the non-dimensional parameter proportional to the droplet's surface regression rate as it vaporizes; α_l is the thermal diffusivity of the liquid phase; $\dot{Q}_l$ is the heat transferred into the liquid; $\overline{Y_N} = (Y_N - Y_{N,0})/Y_{N,0}$ is the normalized mass fraction of the solute; k_l is the thermal conductivity of the liquid phase; $D_{v,za}$ is the mass diffusivity of solute in solvent; and $Pe_l (= r_s |U_g - U_p|/\alpha_l)$ and $Le_l (= D_{v,za}/\alpha_l)$ are the Péclet number and Lewis number of the liquid phase, respectively.

The above set of equations of the model show that the liquid-phase transport affects the temperature and concentration at the droplet surface. This, in turn, affects the evaporation rate and, thus, the droplet size. The droplet size, on the other hand, determines the drag forces, which control the velocity and acceleration of the droplet. The instantaneous droplet velocity affects the heat and mass transfer in the gas phase and, hence, the evaporation rate. Both gas-phase and liquid-phase properties play critical roles in determining the relative effects of these complex coupled processes. In summary, the evaporation of an isolated droplet moving in the gas phase, indeed, involves complex coupled processes.

All the above equations (2.1)–(2.23) are solved numerically, for both external vapour and internal liquid regions. However, in order to solve the liquid phase, the

boundary conditions presented in (2.22) and (2.23) need values from the vapour-phase solution. Therefore, a numerical integration method using a forward marching scheme is implemented to solve (2.1). Moreover, the instantaneous droplet radius (2.8) is also computed by a forward marching scheme using the mass flux $\dot{m}$ generated from (2.9). Furthermore, $\dot{Q}_l$ is solved using Spalding heat transfer number B_T, and both $\dot{Q}_l$ and $\dot{m}$ are employed in the boundary conditions (2.22) and (2.23).

After deriving the boundary conditions from the vapour-phase solution, the energy (2.20) and species (2.22) conservation equations of the droplet's liquid phase along with the boundary conditions (2.22) and (2.23) are numerically computed by a fully implicit iterative finite difference scheme called standard second-order Peaceman–Rachford alternating direction implicit method (Peaceman & Rachford 1955). The details of the numerical algorithm used in this work can be found in Majee *et al.* (2021). The consideration of an implicit scheme guarantees an unconditionally stable method. It is to be noted that the liquid phase inside the droplet was solved using a polar (r–θ) coordinate system, where both dimensions were discretized using an equal number (20 for this study) of grid points, leading to $\Delta\eta = 0.05$ and $\Delta\theta = 0.157$ being taken for the entire simulation process. We have performed a grid convergence study using various grid sizes (see the supplementary material for details). We used a time step of $\Delta t = 0.0001$, which is short enough to capture the transport processes. The property values used for this study can be found in the supplementary material.

3. Results and discussion

As mentioned before, the primary goal of this work is to assess the response in droplet evaporation rate under various degrees of oscillations in gas-phase velocity, given by (2.7). This will be attained by modulating the frequency (f) and amplitude (a) of the oscillation. As for the binary droplet, we assumed that it contains 1 % (w/w) of NaCl (solute) dissolved in water (solvent). Here, we note that a wide range of solute–solvent combinations can be selected for such a study. However, we chose the NaCl solution because (1) it is easily available for experimental validation and (2) it closely resembles surrogate respiratory fluids (Vejerano & Marr 2018; Basu *et al.* 2020). Similarly, a wide range of ambient (temperature and humidity) conditions could be selected for this study. However, we used conditions that closely resemble that of our ambient air ($T_{amb} = 301$ K and $RH_{amb} = 48$ %).

3.1. *Model validation*

To validate the model, we first compare the numerical result with a simple experimental set-up. The experiments were conducted by measuring the evaporation rate of an isolated acoustically levitated droplet with 1 % (w/w) NaCl aqueous solution in 301 ± 0.2 K ambient temperature and $48\% \pm 1\%$ relative humidity. For these experiments, the droplets were at the same temperature as the surrounding air (301 K). Air vortex rings were generated with amplitude $a = 1.9$ m s^{-1} and frequency $f = 5$ Hz and are made to interact with the levitated droplet of initial diameter $D_0 = 1.8$ mm. The mean flow in the experimental set-up is 0.3 m s^{-1}. The details of these experiments are provided in Sharma, Singh & Basu (2021) and Sharma *et al.* (2022). Experimentally, we can only measure the droplet diameter as a function of time, which has been compared with the model for two cases, i.e. with the vortex (unsteady case) and without the vortex (steady case). Since the precipitation kinetics was not included in the current approach, the comparison
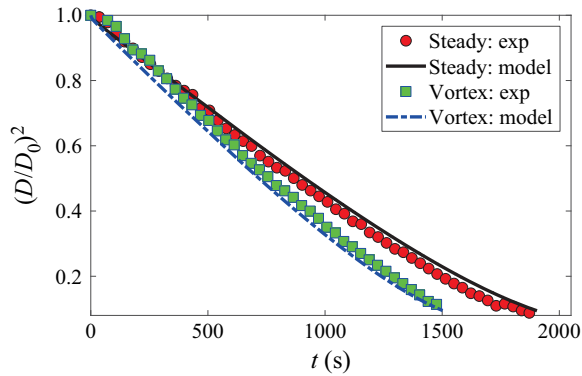
Figure 1. Model validation: comparison of diameter regression, $(D/D_0)^2$, between experimental (levitated droplet) and model data. 'Steady' represents experiments with no vortical flow. 'Vortex' represents experiments with vortical flow over a levitated droplet. In experiments, the initial droplet diameter is $D_0 = 1.8$ mm.

was performed until the maximum local concentration of the solution (NaCl in this case) reached the critical value $Y_{N,S}$ ($= 0.393$ for NaCl). Nevertheless, figure 1, which shows the $(D/D_0)^2$ versus t comparisons between the experiments and the model, confirms that they show reasonably good agreement. Similar agreements were also observed for other amplitude and frequency cases. Thus, we are confident that the model can capture the effects of unsteady gas flow on the evaporation dynamics of an isolated droplet.

3.2. *Evaporation dynamics of the droplet*

In the remainder of this article, we discuss the results from the model to illustrate the effect of a broad range of periodic oscillations in the gas-phase velocity on the evaporation dynamics of an isolated droplet. As mentioned before, we will keep the ambient conditions fixed with $RH_{amb} = 48\%$ and $T_{amb} = 301$ K. The initial droplet temperature was taken as 303 K, which closely resembles the temperature of respiratory droplets ejected during respiratory events (Carpagnano *et al.* 2017). To avoid a negative gas-phase velocity, the mean velocity of the gas phase was kept equal to the amplitude of the gas-phase oscillation, i.e. $U_{g,0} = a$.

We now present the diameter regression rate for various degrees of flow oscillation for two different droplet sizes. First, we compare the evaporation dynamics of a 100 μm droplet under various frequencies of oscillation at amplitude (a) of 0.1 m s^{-1} (figure 2a) and 1 m s^{-1} (figure 2b). We observed that, for a lower amplitude of perturbation ($a = 0.1$ m s^{-1}), the deviation in $(D/D_0)^2$ with the steady ($a = 0$) case is minimal compared with the high-amplitude ($a = 1$ m s^{-1}) case. Although, with an increase in frequency, the evaporation time becomes shorter for the low-amplitude oscillations, the difference between various frequencies is minimal (figure 2a). For larger amplitude, however, we see almost 30 % decrease in time for $(D/D_0)^2$ to reach 0.1 (approximately when precipitation is triggered) for $f = 30$ Hz compared with $f = 1$ Hz, as shown in figure 2(b).

Next, we compare the same amplitude and frequency of oscillations for a larger droplet ($D_0 = 594$ μm) in figure 2(c,d). We observe similar behaviour, in that an increase in amplitude and frequency increases the evaporation rate. However, for both amplitudes, we do not observe significant changes in evaporation rate across various frequencies from
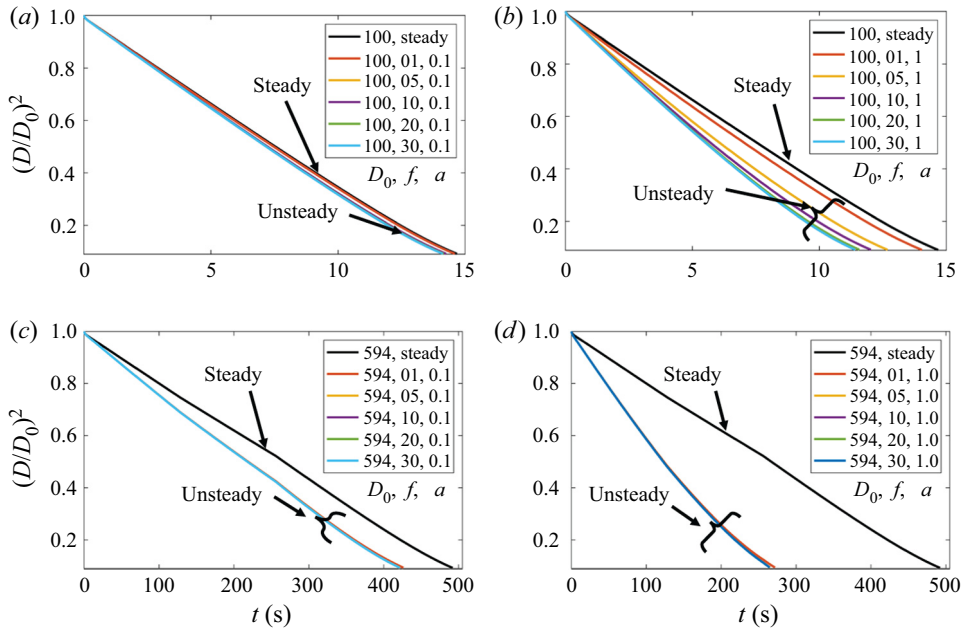
956 A17-9

Figure 2. Normalized droplet diameter as a function of time for various combinations of initial droplet diameters (D_0), amplitude (a) and frequency (f) of gas-phase oscillation: (a) $D_0 = 100\,\mu m$ and $a = 0.1\,m\,s^{-1}$; (b) $D_0 = 100\,\mu m$ and $a = 1\,m\,s^{-1}$; (c) $D_0 = 594\,\mu m$ and $a = 0.1\,m\,s^{-1}$; and (d) $D_0 = 594\,\mu m$ and $a = 1\,m\,s^{-1}$. Legends: 'steady', no gas-phaseoscillation; D_0, initial droplet diameter in μm; f, frequency in Hz; and a, amplitude in $m\,s^{-1}$.

1–30 Hz. Nevertheless, the evaporation is much faster with oscillations (non-zero a) than the steady ($a = 0$) case (14 % for $a = 0.1\,m\,s^{-1}$ and 40 % for $a = 1\,m\,s^{-1}$). The cause of such varying influence of oscillation on the evaporation rate for different droplet sizes and oscillation parameters will be discussed later in the context of the modified Reynolds number.

3.3. *Velocity of gas phase and droplet motion*

The comparisons in the previous subsection show that the effect of oscillation in gas-phase velocity on the evaporation rate is nonlinear. We note that the evaporation rate of the droplet strongly depends on the Nusselt and Sherwood numbers ((2.9) and (2.10)), which depend on the droplet Reynolds numbers ((2.11)–(2.16)), and hence on the relative velocity between the droplet and the surrounding gas phase (2.5). Thus, we investigate the effects of oscillation in gas-phase velocity on the bulk velocity of the droplet. In figures 3 and 4, we compare the instantaneous gas-phase velocity (U_g) and droplet velocity (U_p) during the evaporation process for two different droplet diameters and frequencies of oscillation. In both cases, the mean velocity ($U_{g,0}$) and amplitude (a) of the gas-phase flow were maintained to be $1\,m\,s^{-1}$.

For smaller droplets ($D_0 = 100\,\mu m$) and lower-frequency oscillation ($f = 5\,Hz$), we observe the droplet velocity (U_p) to exhibit a periodic behaviour as well (figure 3). Figure 3(b), which shows an expanded view of the initial 1 s of the droplet lifetime, confirms that, initially, the amplitude of the induced oscillation in the U_p has an amplitude
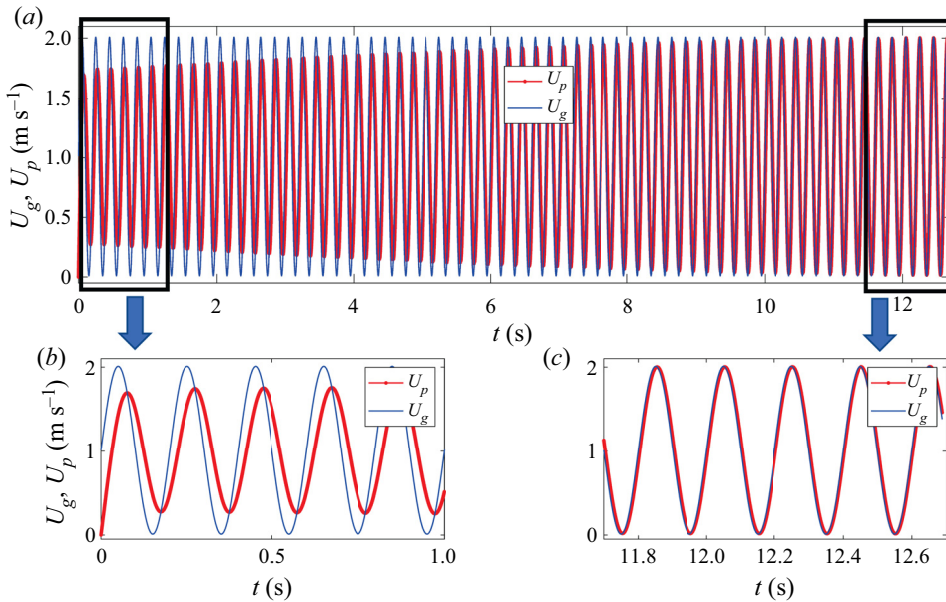
956 A17-10

Figure 3. The instantaneous velocities of the gas phase (U_g) and the droplet (U_p) as functions of time for initial droplet size $D_0 = 100\,\mu\text{m}$. The gas-phase oscillation has amplitude $a = 1\,\text{m s}^{-1}$ and frequency of $f = 5\,\text{Hz}$.
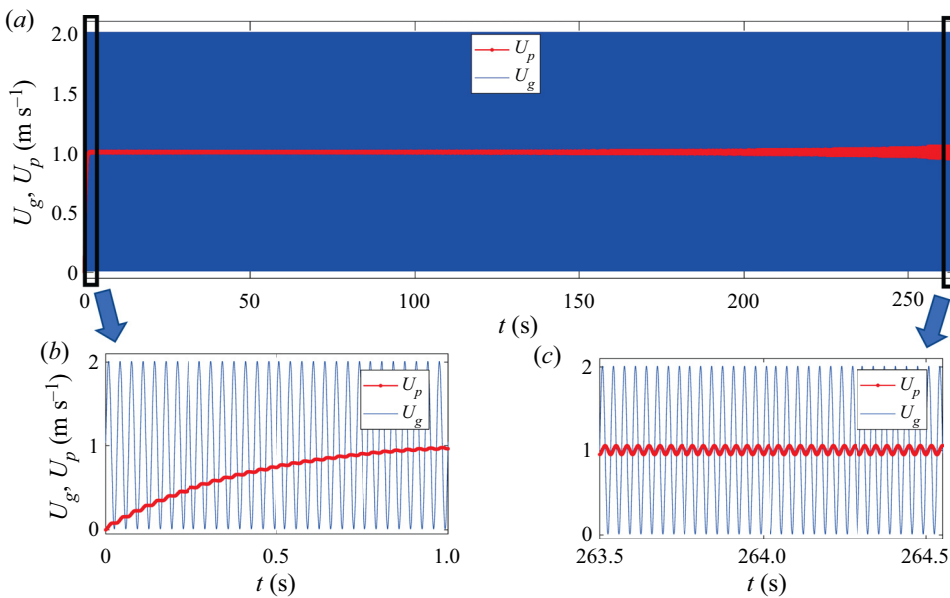

Figure 4. The instantaneous velocities of the gas phase (U_g) and the droplet (U_p) as functions of time for initial droplet size $D_0 = 594\,\mu\text{m}$. The gas-phase oscillation has amplitude $a = 1\,\text{m s}^{-1}$ and frequency of $f = 30\,\text{Hz}$.

slightly smaller than that of the gas phase, and that there exists a phase lag. However, at a later stage (figure 3c), the difference between the two velocities, gas phase (U_g) and droplet (U_p), becomes negligible, and their oscillations become almost identical in both phase and amplitude.

On the other hand, for a larger droplet ($D_0 = 594\,\mu\text{m}$) and higher frequency ($f = 30\,\text{Hz}$) of oscillation, we observe different dynamics (figure 4). In particular, the oscillation in droplet velocity takes longer to attain that of the gas phase. Furthermore, we observe much slower growth in the amplitude of oscillation in U_p, which never grows beyond 10 % before precipitation is triggered ($\sim$265 s). We also observe a consistent phase lag between the oscillation in U_g and U_p.

3.4. *Theoretical scaling analysis*

In this section, we present a time-scale analysis to understand the observed dynamics of induced oscillation in the droplet velocity (U_p). For gas-phase oscillation of $U_g = U_{g,0} + a\sin(2\pi ft)$, we can evaluate the induced oscillation in droplet velocity by integrating the equation for drag (2.6) with the initial condition of $U_p = 0$ at $t = 0$ (initial droplet velocity is zero). We recall the definitions of the drag coefficient ($C_D = 24/Re_p$) and Reynolds number ($Re_p = 2\rho_g|U_g - U_p|r_s/\mu_g$). We can also define $\tau = (\rho_l r_s^2)/\mu_g$ as the response time for a spherical droplet in a viscous flow, and $t_g = 1/f$ as the characteristic time scale for gas-phase oscillation. The droplet response in an unsteady flow is characterized by Stokes number $St = \tau/t_g$ (Crowe, Sommerfeld & Tsuji 1998), which represents the ratio of the characteristic time scale for droplet response (τ) to that of the external flow (t_g). In the context of our study with oscillatory gas-phase velocity, the Stokes number can be written as $St = \tau f$.

Now substituting these definitions in (2.6), we get a non-dimensional drag equation:

$$\frac{\mathrm{d}((U_p - U_{g,0})/a)}{\mathrm{d}(t/t_g)} = -\frac{9}{2St}\left(\frac{U_p - U_{g,0}}{a}\right) + \frac{9}{2St}\sin\left(2\pi\frac{t}{t_g}\right). \qquad (3.1)$$

In the equation above, we notice that the non-dimensional droplet velocity, $(U_p - U_{g,0})/a$, depends on St, which includes the effect of instantaneous droplet radius and t/t_g, a non-dimensional time.

For simplicity, we restrict the analysis to a non-evaporating spherical droplet, and, hence, the droplet radius (r_s) and the Stokes number (St) are assumed to be constant. Later, we will discuss the effect of this assumption on the obtained results. With this assumption, we can integrate (3.1) to find an explicit form of the non-dimensional droplet velocity:

$$\frac{U_p - U_{g,0}}{a} = \frac{\sin(2\pi(t/t_g) - \phi)}{\sqrt{1 + (16\pi^2 St^2/81)}} + \left(-\frac{U_{g,0}}{a} + \frac{4\pi St/9}{(1 + (16\pi^2 St^2/81))}\right)\mathrm{e}^{-9t/(2t_g St)}, \qquad (3.2)$$

where $\phi = \tan^{-1}(4\pi St/9)$.

Equation (3.2) depicts the response in velocity of a non-evaporating spherical droplet when the surrounding gas phase has an oscillatory perturbation. The first term on the right-hand side represents the induced oscillation in droplet velocity. We notice that the frequency of the induced oscillation in droplet velocity is the same as the gas-phase perturbation (f or $1/t_g$), while the non-dimensionalized amplitude of the induced oscillation is $A_{osc} = 1/\sqrt{1 + (16\pi^2 St^2/81)}$. The induced oscillation in the droplet velocity lags the oscillation in gas-phase velocity by a phase angle, ϕ. The second term
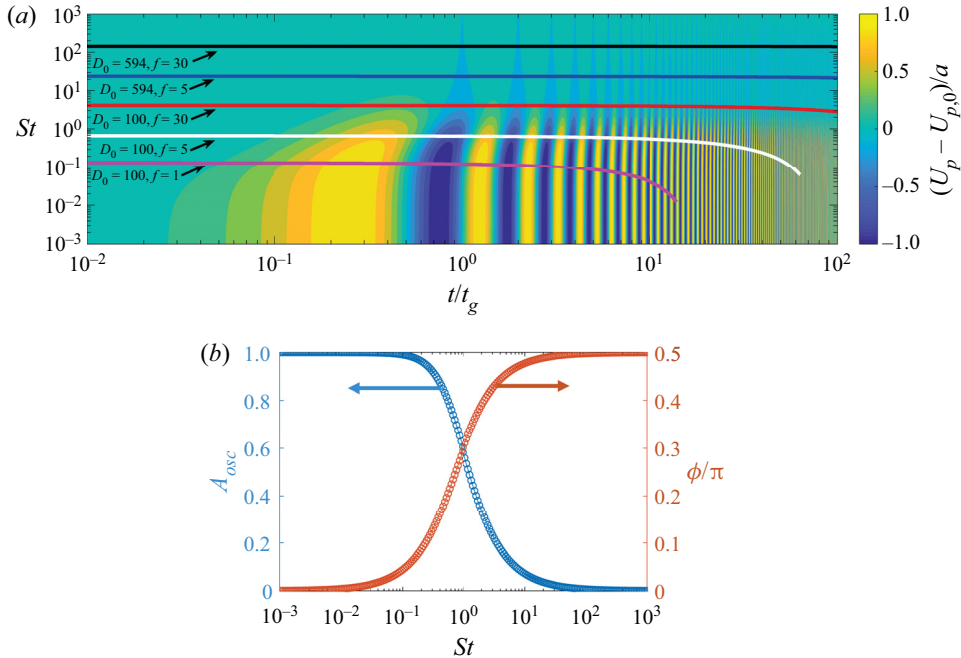
956 A17-12

Figure 5. (*a*) Contour plot of non-dimensional change in droplet velocity, $(U_p - U_{p,0})/a$, with Stokes number (St) and non-dimensional time (t/t_g), where t_g is the gas-phase perturbation time. History of Stokes number (St) for different initial diameters and frequencies is plotted on the contour map. Legend: D_0, initial diameter in μm; and f, frequency of gas-phase oscillation in Hz. For all five cases, the amplitude of the gas-phase oscillation is $a = 1$ m s^{-1}. (*b*) Variation in amplitude ($A_{osc} = 1/\sqrt{1 + (16\pi^2 St^2/81)}$) and phase lag ($\phi = \tan^{-1}(4\pi St/9)$) of the induced oscillation in non-dimensional droplet velocity, $(U_p - U_{g,0})/a$, as a function of Stokes number (St).

on right-hand side shows the effect of viscous drag, which exponentially reduces the difference between the mean velocities of the droplet and the gas phase. It is worth noting that, for a steady gas-phase flow (i.e. $a = 0$), the oscillatory term vanishes, and (3.2) reduces to the classical exponential relation for a non-evaporating droplet (or spherical object) in a gaseous flow field, $U_{p,0} = U_{g,0}(1 - e^{-9t/(2t_g St)})$.

To graphically illustrate the droplet response expressed in (3.2), we present the contour plot of the normalized droplet velocity, $(U_p - U_{p,0})/a$, for a large range of St (Y-axis) and non-dimensional time t/t_g (X-axis) in figure 5(*a*). Since $U_{p,0}$ is the droplet velocity in a steady gas-phase flow, $(U_p - U_{p,0})/a$ measures the modification in droplet velocity due to the unsteady oscillations in the gas phase. Furthermore, we also plotted the amplitude (A_{osc}) and phase (ϕ) of the induced oscillation in droplet velocity as a function of St in figure 5(*b*).

From the contour plot (figure 5*a*), we can see that, for a small St ($\ll 1$), the droplet velocity, $(U_p - U_{p,0})/a$, exhibits a periodic behaviour with time, expressed by the colour bands in the horizontal direction. The periodicity in the colour band appears to be non-uniform due to the log scale used on the X-axis. A dominant periodic behaviour at small St is expected, as the second term on the right-hand side of (3.2) is small. The amplitude of the induced oscillation for this case ($St \ll 1$) is also high and close to that of the gas-phase perturbation ($A_{osc} \approx 1$), as seen in figure 5(*b*). As St increases and approaches 1, the periodic pattern still exists, but the difference between the maximum and

minimum instantaneous velocity (colour variation in figure 5*a*) becomes weaker due to the reduced amplitude of the induced oscillation (A_{osc} in figure 5*b*). We also notice that the maximum velocity zones (bright yellow zones) in the contour plot shift towards the right. This is the outcome of increased phase lag ϕ between droplet and gas-phase velocities with increasing *St* (figure 5*b*). For very large *St* ($\gg 1$), the denominator of the first term on the right-hand side of (3.2) becomes significantly greater than unity. As such, the amplitude of the oscillation becomes minimal (A_{osc} in figure 5*b*). This is why the colour variation in the horizontal direction (as a function of time) diminishes in the top half of the contour plot (*St* $\gg 1$ in figure 5*a*).

The above analyses can also be performed by considering the variation in droplet radius due to evaporation. However, such an approach, shown in Appendix A, does not lead to a closed-form expression for the droplet velocity. Furthermore, it can be shown (see Appendix A) that the difference in the change in droplet velocity due to oscillation, ($U_p - U_{p,0}$)/a, evaluated using the two approaches (with and without the assumption of constant droplet radius) is relatively insignificant. Hence, we used the constant droplet assumption for the rest of the study.

Now, to illustrate the range of *St* experienced by the evaporating droplets, we plotted the instantaneous *St* obtained from the simulation of various cases on the theoretical contour plot in figure 5(*a*). Since the droplet diameter and, hence, τ decrease due to evaporation, the *St* value shows a downward decreasing trend with non-dimensional time (t/t_g). We observe that the cases with a small initial diameter ($D_0 = 100\ \mu$m) and lower-frequency oscillations ($f = 1$ and 5 Hz) experience low *St* and, hence, large-amplitude oscillations in velocity (figure 5*a*). This effect is also observed in figure 3, where we showed that, for $D_0 = 100\ \mu$m and $f = 5$ Hz, the amplitude of oscillation in droplet velocity quickly attains that of the gas-phase velocity. As the frequency of oscillation in gas-phase velocity (f) increases, *St* increases, reducing the amplitude of induced oscillation in droplet velocity ($f = 1$, 5 and 30 Hz in figure 5*a*). For larger droplets ($D_0 = 594\ \mu$m), the *St* value becomes significantly greater than unity, and hence they do not exhibit significant induced oscillations in velocity. For $D_0 = 594\ \mu$m and $f = 30$ Hz, we observe a weak response, and hence the amplitude becomes inconsequential to the frequency change (figure 4).

Next, we will assess the effect of oscillation in gas-phase flow on Re_p, which, in turn, affects the evaporation rate. Since the external conditions are kept constant in our simulations, the changes in diameter reduction rate observed in figure 2(*a*–*d*) are through the Sherwood (Sh^*) and Nusselt (Nu^*) numbers in (2.9) and (2.10), respectively. Equations (2.11)–(2.16) subsequently show that an increase in Re_p increases both Sh^* and Nu^*, and hence the evaporation rate. Since the Reynolds number (Re_p) is defined based on the relative velocity between the gas phase and the droplet, one can evaluate the induced Re_p due to gas-phase velocity oscillation by substituting U_p (3.2) and U_g (2.7) into (2.5). Similarly, it is also possible to evaluate the Reynolds number of the droplet without the gas-phase oscillation ($a = 0$) as $Re_{p,0} = 2\rho_g|U_{g,0} - U_{p,0}|r_s/\mu_g$. Clearly, higher (or lower) values of the ratio $Re_p/Re_{p,0}$ signify stronger (or weaker) effects of gas-phase oscillation on the evaporation rate compared with the steady condition ($a = 0$).

Figure 6(*a*) shows the contours of this ratio ($Re_p/Re_{p,0}$) for a range of *St* and normalized time, t/t_g. Based on the colour, the map can be divided (almost diagonally) into two parts separated by the dotted line, St_{crit}. The top-left half, where the instantaneous values of $Re_p/Re_{p,0}$ are close to unity (10^0 in the plot), represents a zone where the relative effects of gas-phase oscillation on *Re* with respect to $Re_{p,0}$ is small, and hence can be characterized
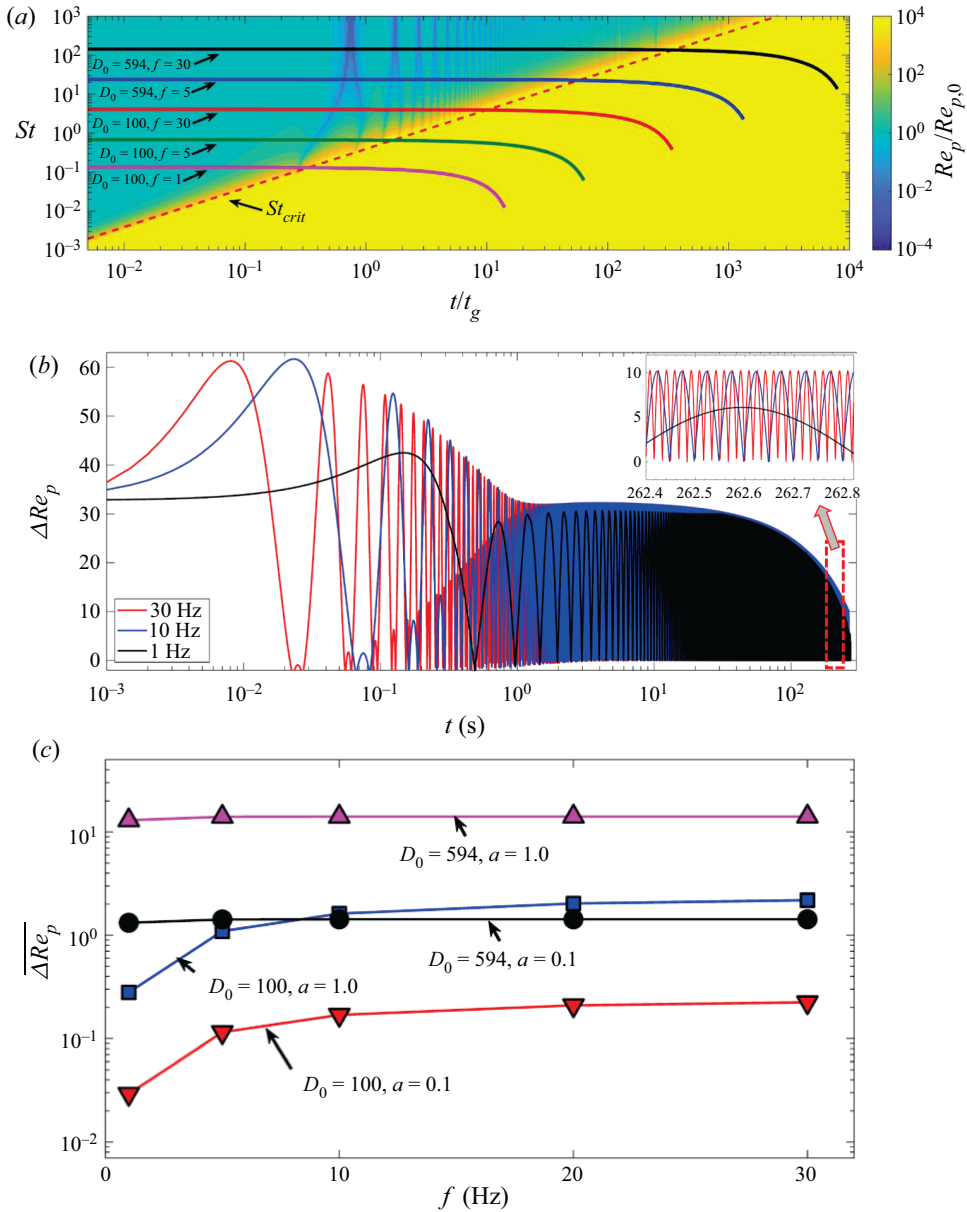
Figure 6. (*a*) Contour plot for $Re_p/Re_{p,0}$ with Stokes number (St) and non-dimensional time (t/t_g), where t_g is the gas-phase perturbation time. History of Stokes number (St) for different initial diameters and frequencies is plotted on the contour map. Legend: D_0, initial diameter in µm; and f, frequency of gas-phase oscillation in Hz. For all five cases, the amplitude of the gas-phase oscillation is $a = 1$ m s^{-1}. (*b*) Time history of changes in droplet Reynolds number due to gas-phase oscillation ($\Delta Re_p = Re_p - Re_{p,0}$) for amplitude $a = 1$ m s^{-1}, frequencies ($f = 1$, 10 and 30 Hz). The initial droplet diameter (D_0) is 594 µm. (*c*) The average changes in droplet Reynolds number due to gas-phase oscillation ($\overline{\Delta Re_p}$, averaged ΔRe_p) as a function of frequency f of gas-phase oscillation for different amplitudes (a in m s^{-1}) and initial droplet diameters (D_0 in µm).

as a 'zone of silence'. The change in droplet velocity ($U_p - U_{p,0} \approx 0$) due to gas-phase oscillation is, indeed, weak, as observed in figure 5(a). Furthermore, under steady flow conditions, the relative velocity between the droplet and the gas phase (hence, $Re_{p,0}$) is high.

On the other hand, the bottom-right half of figure 6(a) represents a zone where $Re_p/Re_{p,0}$ has a very high value, and hence can be characterized as a 'zone of influence'. In this regime, droplet velocity (U_p) displays strong oscillatory behaviour, as shown in figure 5(a). Furthermore, under steady gas-phase flow ($a = 0$), the differences between the droplet velocity become small (and hence $Re_{p,0} \to 0$). Consequently, for a given t/t_g, the transition between the 'zone of silence' and the 'zone of influence' can be marked by a critical Stokes number (St_{crit}) for which $U_{p,0} \to U_{g,0}$. In figure 6(a), a representative transitional boundary is drawn by setting $(U_{p,0} - U_{g,0})/U_{g,0} = 10^{-5}$. The St history from a few simulated conditions are superimposed on the contour plot. We observe that, initially, the droplet starts from the 'zone of silence', but transitions into the 'zone of influence' (figure 6) as time progresses and the droplet becomes smaller due to evaporation.

While $Re_p/Re_{p,0}$ depicts the relative change in Re_p due to oscillation in the gas phase, it is to be recognized that $Re_{p,0} \approx 0$ in the 'zone of influence', and, as such, the ratio becomes large, even for a small Re_p. To circumvent this bias and to assess the true effect on the evaporation rate, one should evaluate their differences, i.e. $\Delta Re_p = Re_p - Re_{p,0}$. In figure 6($b$), we plotted ΔRe_p as a function of time for a given initial droplet size ($D_0 = 594\ \mu\mathrm{m}$) and amplitude ($a = 1\ \mathrm{m\ s}^{-1}$), but for three different frequencies ($f = 1$, 10 and 30 Hz) of gas-phase oscillation. The plot displays large-amplitude oscillations in ΔRe_p at the initial stage. However, the amplitude decays with time and becomes almost constant in the later stage of the droplet lifetime (see inset of figure 6b). This behaviour, indeed, corroborates the dynamics of droplet velocity, U_p, described before.

To estimate an overall change in Re_p due to oscillation in gas-phase flow, we evaluated the mean of ΔRe_p (denoted by $\overline{\Delta Re_p}$) for four combinations of amplitude (a) and initial droplet diameter (D_0) and plotted them as a function of frequency (f) of gas-phase oscillation in figure 6(c). For smaller droplets ($D_0 = 100\ \mu\mathrm{m}$) and lower amplitude ($a = 0.1\ \mathrm{m\ s}^{-1}$) of oscillation, the $\overline{\Delta Re_p}$ value is small ($\sim 10^{-1}$), which explains why we did not observe significant changes in evaporation rate among various frequencies as shown in figure 2(a). On the other hand, for larger amplitude ($a = 1\ \mathrm{m\ s}^{-1}$), $\overline{\Delta Re_p}$ is relatively higher (~ 1), and increases with f. Thus, we observed a faster evaporation rate with oscillations, which increases with frequency (figure 2b). Figure 6(c) also confirms that $\overline{\Delta Re_p}$ for larger droplets ($D_0 = 594\ \mu\mathrm{m}$) is higher and remains almost constant for all f, irrespective of the amplitude ($a = 0.1$ and $1\ \mathrm{m\ s}^{-1}$). This explains the observed faster evaporation under unsteady gas-phase flow but the insignificant difference between various frequencies (figure 2c,d) for the larger droplets.

3.5. *Temperature and concentration distributions in the liquid phase*

Since our model includes transport equations for the liquid phase, we can compare the temperature and concentration distributions inside the droplet to illustrate the effect of unsteadiness in gas-phase velocities on the liquid-phase transport. Figures 7 (temperature) and 8 (mass fraction of solute) display the evolutions of the internal dynamics for three instances on the lifetime of a $D_0 = 100\ \mu\mathrm{m}$ droplet and compare them for three different
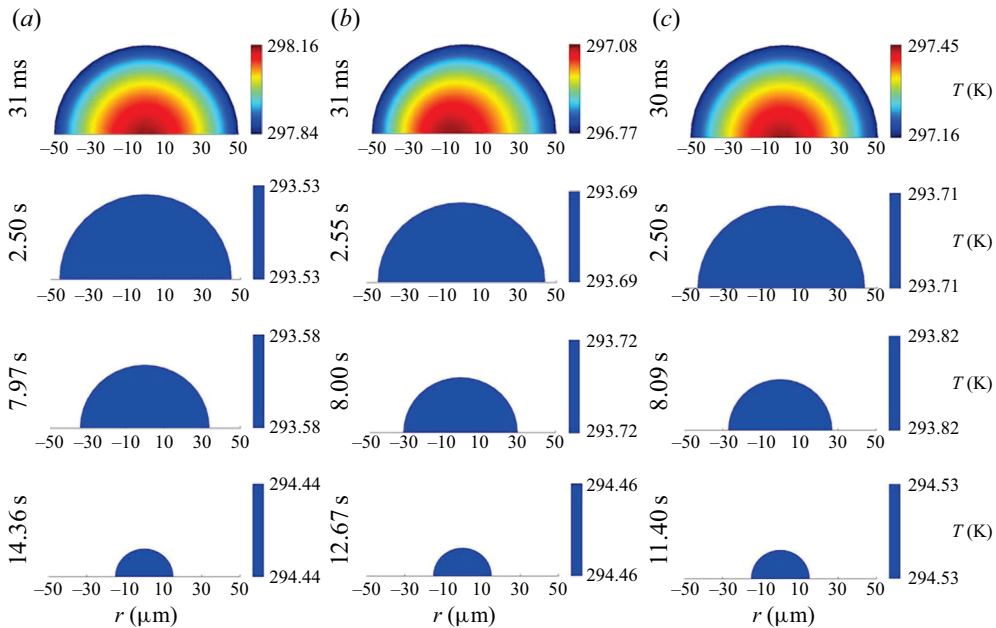
Figure 7. Temperature distribution in the liquid phase at different time steps for $D_0 = 100\,\mu\text{m}$ with initial droplet temperature, $T_0 = 303\,\text{K}$. The ambient condition is $T_{amb} = 301\,\text{K}$ and $RH_{amb} = 48\,\%$. The gas-phase perturbation: (*a*) amplitude, $a = 0.1\,\text{m s}^{-1}$, and frequency, $f = 5\,\text{Hz}$; (*b*) $a = 1\,\text{m s}^{-1}$ and $f = 5\,\text{Hz}$; and (*c*) $a = 1\,\text{m s}^{-1}$ and $f = 30\,\text{Hz}$.

degrees of oscillations in the gas phase. Similar contour plots for $D_0 = 594\,\mu\text{m}$ are shown in figures 9 (temperature) and 10 (mass fraction of solute). Here, we recall that the ambient condition for the simulation was $T_{amb} = 301\,\text{K}$ and $RH_{amb} = 48\,\%$, while the initial droplet temperature was set at 303 K and initial solute (NaCl) concentration dissolved in water was $Y_{N,0} = 1\,\%$.

Figures 7 and 9 depict that, in the early stage of evaporation, the temperature distribution displays a symmetric concentric profile. This is the hallmark of stronger diffusional transport than advective transport of thermal energy (Sirignano 1983; Abramzon & Sirignano 1989; Saha *et al.* 2009*b*) caused by large thermal diffusivity in the liquid phase. The enhanced thermal transport and smaller initial temperature difference between the gas phase and liquid phase enable the droplet to reach the wet-bulb temperature and attain homogeneity in a short duration, as seen in both figures 7 and 9. Owing to the dominant diffusive transport in the liquid phase, the effects of amplitude and frequency of the gas-phase oscillation on the temperature profiles are not significant.

Figures 8 and 10 show the concentration distribution of solute in the liquid phase for two different droplet sizes. We notice that the lower amplitude of gas-phase oscillation ($a = 0.1\,\text{m s}^{-1}$) leads to a diffusion-dominated concentric distribution even in the early stage of droplet lifetime (figures 8*a* and 10*a*). On the other hand, for high-amplitude oscillations ($a = 1\,\text{m s}^{-1}$), a recirculation pattern was formed inside the droplet, which resembles the internal flow pattern (Hill's spherical vortex) (figures 8*b*,*c* and 10*b*,*c*). This indicates strong advective transport. The relative strength between advective and diffusive mass transport can be expressed by the Péclet number, $Pe_l = Re_l Sc$, where Sc is the Schmidt number (roughly constant). The liquid-phase Reynolds number, Re_l, is
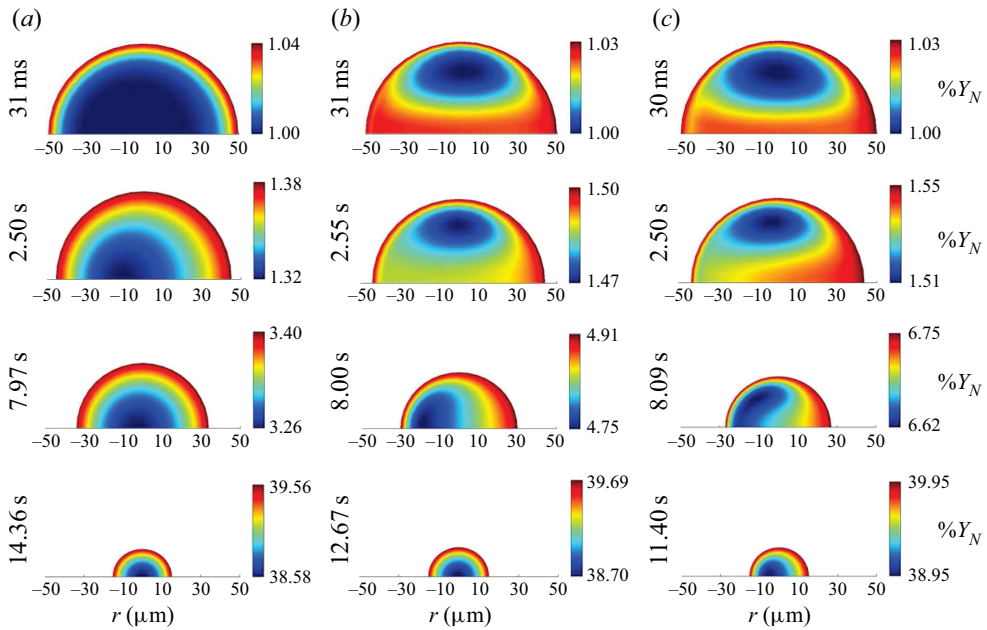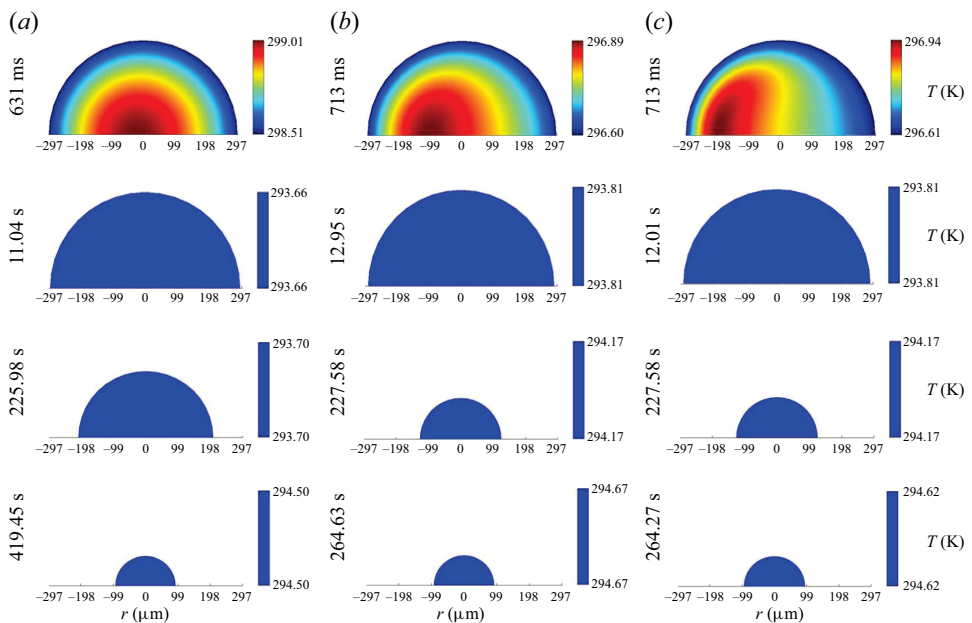
Figure 8. Solute concentration distribution in the liquid phase at different time steps for $D_0 = 100\ \mu$m with initial droplet temperature, $T_0 = 303$ K. The ambient condition is $T_{amb} = 301$ K and $RH_{amb} = 48\,\%$. The gas-phase perturbation: (*a*) amplitude, $a = 0.1$ m s^{-1}, and frequency, $f = 5$ Hz: (*b*) $a = 1$ m s^{-1} and $f = 5$ Hz: and (*c*) $a = 1$ m s^{-1} and $f = 30$ Hz.

Figure 9. Temperature distribution in the liquid phase at different time steps for $D_0 = 594\ \mu$m with initial droplet temperature, $T_0 = 303$ K. The ambient condition is $T_{amb} = 301$ K and $RH_{amb} = 48\,\%$. The gas-phase perturbation: (*a*) amplitude, $a = 0.1$ m s^{-1}, and frequency, $f = 5$ Hz: (*b*) $a = 1$ m s^{-1} and $f = 5$ Hz; and (*c*) $a = 1$ m s^{-1} and $f = 30$ Hz.

956 A17-18
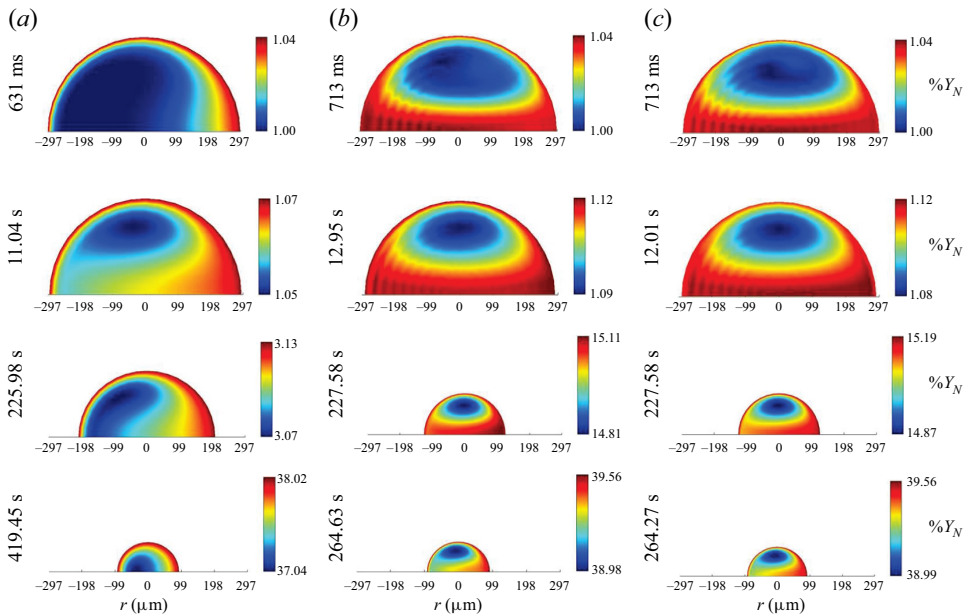
Figure 10. Solute concentration distribution in the liquid phase at different time steps for $D_0 = 594$ µm with initial droplet temperature, $T_0 = 303$ K. The ambient condition is $T_{amb} = 301$ K and $RH_{amb} = 48\%$. The gas-phase perturbation: (*a*) amplitude, $a = 0.1$ m s^{-1}, and frequency, $f = 5$ Hz; (*b*) $a = 1$ m s^{-1} and $f = 5$ Hz; and (*c*) $a = 1$ m s^{-1} and $f = 30$ Hz.

defined based on the (liquid-phase) velocity at the vapour–liquid interface (U_s) driven by gas-phase flow or Re_p ((2.17) and (2.18)). As shown in figure 5, an increase in the amplitude of oscillation increases Re_p, and hence Pe_l. This is why we observe stronger advective transport for the higher amplitude of gas-phase oscillation (figures 8 and 10) in the early stage of evaporation. As the droplet evaporates, Re_p decreases. As such, both Pe_l and the advective transport in the liquid phase become weaker, resulting in more concentric iso-concentration lines for $D_0 = 100$ µm droplets (figure 8*b,c*). However, for $D_0 = 594$ µm, Re_l and Pe_l remain comparatively higher throughout the droplet lifetime due to larger droplet diameters. Thus, convective transport remains strong, as reflected in vortical isocontours in figure 10(*b,c*).

It is to be noted that, for the conditions used in this study, the droplet exhibits almost uniform temperature and concentration distributions except for the initial period of evaporation. One can also employ the rapid mixing model for the liquid phase (Law 1976), which assumes an infinitely fast diffusion process that leads to homogeneous temperature and concentration inside the droplet. Since our goal is to provide a framework that can be used for a wide range of ambient conditions, we used the detailed liquid-phase transport model proposed by Abramzon & Sirignano (1989).

4. Summary and outlook

In summary, we have presented a numerical investigation assessing the effect of oscillation in gas-phase velocity on the evaporation rate of an isolated binary droplet. Using a detailed one-way coupled two-phase model, we demonstrated that the evaporation rate increases with the amplitude and frequency of gas-phase oscillations and that the influence

of oscillation becomes stronger for larger droplets. Subsequently, a scaling analysis illustrated that the oscillation in gas-phase velocity induces an oscillatory response in the instantaneous droplet velocity, whose amplitude, frequency and phase lag depend on three time scales, leading to two non-dimensional parameters, Stokes number (ratio of inertial versus time period of oscillation) and normalized time (ratio of physical time and the time period of oscillations).

Subsequently, a theoretical estimate of augmentation in the droplet Reynolds number was performed based on the scaling of the induced droplet velocity. Furthermore, the effects of the amplitude and the frequency of oscillation in gas-phase velocity on the increase in effective Reynolds number were evaluated. An increase in Reynolds number was shown to induce faster gas-phase transport at the droplet interface, which explains the enhanced evaporation rate for higher amplitude and frequency of gas-phase oscillations. Finally, we discussed transport processes inside the droplet to show that gas-phase oscillation has a minimal effect on liquid-phase thermal transport due to high thermal diffusivity and hence diffusive transport. The solute concentration, on the other hand, shows stronger advective transport for a larger amplitude of oscillation, confirmed by enhanced liquid-phase Péclet number.

Author ORCIDs.
- Sreeparna Majee https://orcid.org/0000-0001-6128-3890;
- Abhishek Saha https://orcid.org/0000-0001-9619-6623;
- Saptarshi Basu https://orcid.org/0000-0002-9652-9966.

Author contributions. Conceptualization – A.S. and S.B.; methodology – A.S., S.B. and S.M.; investigation – S.M. and A.S.; visualization – S.M. and A.S.; funding acquisition – A.S. and S.B.; supervision – A.S. and S.B.; writing (original draft) – S.M. and A.S.; and writing (editing and revision) – S.M., A.S. and S.B.

Data availability statement. The data can be made available upon reasonable request.

Appendix A. Effect of evaporation on the scaling analyses

In § 3.4, we used the approximation of constant droplet radius for the scaling analyses. Now, we will perform the analyses without assuming a constant droplet radius. It is to be recognized that a variation in droplet size essentially results in a variation in St with time in (3.1). To find a theoretical expression for changes in droplet radius or Stokes number, we can assume that the droplet quickly attains a steady state (constant temperature and concentration). Thus, the d^2 law (Law 1982), $\mathrm{d}r_s^2(t)/\mathrm{d}t = -K_v$, can be applied to evaluate instantaneous droplet radius. Here, the constant K_v can be expressed using B_M, i.e. $K_v = 2(\rho_g/\rho_l)\alpha_g\ln(1 + B_M)$. It is to be noted that a similar expression for K_v can also be derived using B_T (Law 1982). The Spalding mass (or heat transfer) numbers B_M (or B_T) can be evaluated based on the final (steady-state) droplet temperature. Here, α_g is the gas-phase thermal diffusivity.
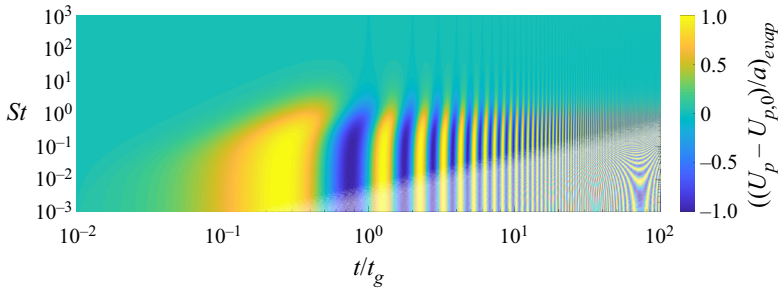
Figure 11. Contour plot of non-dimensional droplet velocity, $(U_p - U_{p,0})/a$, with Stokes number (St) and non-dimensional time (t/t_g), where t_g is the gas-phase perturbation time. Here, we used the d^2 law to assess the change in evaporating droplet radius.
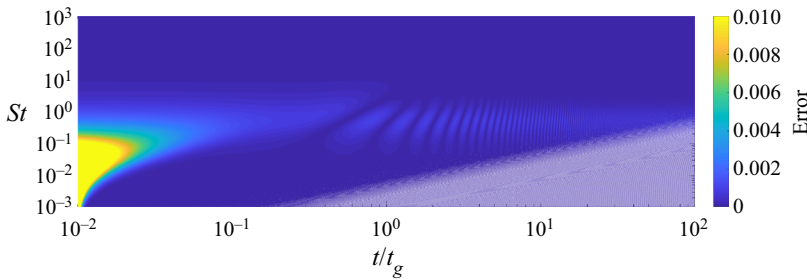

Figure 12. Contour plot of the error, defined as the absolute difference in $(U_p - U_{p,0})/a$ using the constant diameter and variable diameter.

It can be seen that K_v dictates the droplet lifetime or evaporation rate. For the ambient conditions used for this study, K_v has a value of approximately 2.2×10^{-10} m^2 s^{-1}. However, for hot–dry and cold–humid ambient conditions, K_v is expected to be larger and smaller, respectively. By substituting the Stokes number ($St = \tau/t_g$) in the d^2 law, we find a regression equation for the Stokes number:

$$\frac{\mathrm{d}St}{\mathrm{d}(t/t_g)} = -K_v(\rho_l/\mu_g). \tag{A1}$$

To obtain a time history of droplet velocity, one has to solve the coupled ordinary differential equations (ODEs) represented by (3.1) and (A1). Unfortunately, a compact closed-form solution does not exist for this set of ODEs. However, we can solve these equations numerically.

Based on the analysis with the evaporating droplet, we present the contour plot of the normalized droplet velocity, $(U_p - U_{p,0})/a$, for a large range of St (Y-axis) and non-dimensional time, t/t_g (X-axis) in figure 11.

Visual comparison of figures 5(a) and 11 suggests that the results are practically identical, although the former used the constant radius approximation and the latter did not. We also plot the error, defined as the absolute differences between the constant-radius and variable-radius methods, in figure 12. The difference is less than 1 %, confirming that the constant droplet size assumption is satisfactory.

956 A17-21

REFERENCES

ABRAMZON, B. & SIRIGNANO, W.A. 1989 Droplet vaporization model for spray combustion calculations. *Intl J. Heat Mass Transfer* **32** (9), 1605–1618.

AGGARWAL, S.K., PARK, T.W.M. & KATTA, V.R. 1996 Unsteady spray behavior in a heated jet shear layer: droplet-vortex interactions. *Combust. Sci. Technol.* **113** (1), 429–449.

AGGARWAL, S.K. & PENG, F. 1995 A review of droplet dynamics and vaporization modeling for engineering calculations. *Trans. ASME J. Engng Gas Turbines Power* **117** (3), 453–461.

BADER, A., KELLER, P. & HASSE, C. 2013 The influence of non-ideal vapor–liquid equilibrium on the evaporation of ethanol/iso-octane droplets. *Intl J. Heat Mass Transfer* **64**, 547–558.

BALACHANDAR, S., ZALESKI, S., SOLDATI, A., AHMADI, G. & BOUROUIBA, L. 2020 Host-to-host airborne transmission as a multiphase flow problem for science-based social distance guidelines. *Intl J. Multiphase Flow* **132**, 103439.

BASU, S. & CETEGEN, B.M. 2008 Modeling of liquid ceramic precursor droplets in a high velocity oxy-fuel flame jet. *Acta Mater.* **56** (12), 2750–2759.

BASU, S., JORDAN, E.H. & CETEGEN, B.M. 2008 Fluid mechanics and heat transfer of liquid precursor droplets injected into high-temperature plasmas. *J. Therm. Spray Technol.* **17** (1), 60–72.

BASU, S., KABI, P., CHAUDHURI, S. & SAHA, A. 2020 Insights on drying and precipitation dynamics of respiratory droplets from the perspective of COVID-19. *Phys. Fluids* **32** (12), 123317.

BERLEMONT, A., DESJONQUERES, P. & GOUESBET, G. 1990 Particle lagrangian simulation in turbulent flows. *Intl J. Multiphase Flow* **16** (1), 19–34.

BHAGAT, R.K., WYKES, M.S.D., DALZIEL, S.B. & LINDEN, P.F. 2020 Effects of ventilation on the indoor spread of COVID-19. *J. Fluid Mech.* **903**.

BIROUK, M. & GOKALP, I. 2006 Current status of droplet evaporation in turbulent flows. *Prog. Energy Combust. Sci.* **32** (4), 408–423.

BORODULIN, V.Y., NIZOVTSEV, M.I. & STERLYAGOV, A.N. 2019 Evaporation of non-ideal binary solution drops. In *Journal of Physics: Conference Series*, vol. 1382, p. 012106. IOP Publishing.

BOUROUIBA, L. 2020 Turbulent gas clouds and respiratory pathogen emissions: potential implications for reducing transmission of COVID-19. *JAMA* **323** (18), 1837–1838.

BOUROUIBA, L. 2021 The fluid dynamics of disease transmission. *Annu. Rev. Fluid Mech.* **53**, 473–508.

BURGER, M., SCHMEHL, R., KOCH, R., WITTIG, S. & BAUER, H.-J. 2006 DNS of droplet–vortex interaction with a karman vortex street. *Intl J. Heat Fluid Flow* **27** (2), 181–191.

CANTWELL, B., KARABEYOGLU, A. & ALTMAN, D. 2010 Recent advances in hybrid propulsion. *Int. J. Energetic Mater. Chem. Propul.* **9** (4), 305–326.

CARPAGNANO, G.E., FOSCHINO-BARBARO, M.P., CROCETTA, C., LACEDONIA, D., SALIANI, V., ZOPPO, L.D. & BARNES, P.J. 2017 Validation of the exhaled breath temperature measure: reference values in healthy subjects. *Chest* **151** (4), 855–860.

CHAUDHURI, S., BASU, S., KABI, P., UNNI, V.R. & SAHA, A. 2020*a* Modeling the role of respiratory droplets in COVID-19 type pandemics. *Phys. Fluids* **32** (6), 063309.

CHAUDHURI, S., BASU, S. & SAHA, A. 2020*b* Analyzing the dominant SARS-CoV-2 transmission routes toward an ab initio disease spread model. *Phys. Fluids* **32** (12), 123306.

CHEN, L., LIU, Z., LIN, Y. & ZHANG, C. 2016 Different spray droplet evaporation models for non-ideal multi-component fuels with experimental validation. *Intl J. Heat Mass Transfer* **94**, 292–300.

CHONG, K.L., NG, C.S., HORI, N., YANG, R., VERZICCO, R. & LOHSE, D. 2021 Extended lifetime of respiratory droplets in a turbulent vapor puff and its implications on airborne disease transmission. *Phys. Rev. Lett.* **126** (3), 034502.

CLEMENS, N.T. & MUNGAL, M.G. 1995 Large-scale structure and entrainment in the supersonic mixing layer. *J. Fluid Mech.* **284**, 171–216.

CLIFT, R., GRACE, J.R. & WEBER, M.E. 2005 *Bubbles, Drops, and Particles*. Courier Corporation.

CROWE, C., SOMMERFELD, M. & TSUJI, Y. 1998 *Multiphase Flows with Droplets and Particles*. CRC Press.

DBOUK, T. & DRIKAKIS, D. 2020 On coughing and airborne droplet transmission to humans. *Phys. Fluids* **32** (5), 053310.

DWYER, H.A., AHARON, I., SHAW, B.D. & NIAMAND, H. 1996 Surface tension influences on methanol droplet vaproiation in the presence of water. In *Symposium (International) on Combustion*, vol. 26, pp. 1613–1619. Elsevier.

DWYER, H.A., SHAW, B.D. & NIAZMAND, H. 1998 Droplet/flame interactions including surface tension influences. In *Symposium (International) on Combustion*, vol. 27, pp. 1951–1957. Elsevier.

FANG, B., CHEN, L., LI, G. & WANG, L. 2019 Multi-component droplet evaporation model incorporating the effects of non-ideality and thermal radiation. *Intl J. Heat Mass Transfer* **136**, 962–971.

GRABOWSKI, W.W. & WANG, L.-P. 2013 Growth of cloud droplets in a turbulent environment. *Annu. Rev. Fluid Mech.* **45**, 293–324.

HARSTAD, K. & BELLAN, J. 1997 Behavior of a polydisperse cluster of interacting drops evaporating in an inviscid vortex. *Intl J. Multiphase Flow* **23** (5), 899–925.

HUBBARD, G.L., DENNY, V.E. & MILLS, A.F. 1975 Droplet evaporation: effects of transients and variable properties. *Intl J. Heat Mass Transfer* **18** (9), 1003–1008.

JAYAWEERA, M., PERERA, H., GUNAWARDANA, B. & MANATUNGE, J. 2020 Transmission of COVID-19 virus by droplets and aerosols: a critical review on the unresolved dichotomy. *Environ. Res.* **188**, 109819.

JORDAN, E.H., JIANG, C. & GELL, M. 2015 The solution precursor plasma spray (SPPS) process: a review with energy considerations. *J. Therm. Spray Technol.* **24** (7), 1153–1165.

KIM, I., ELGHOBASHI, S. & SIRIGNANO, W.A. 1995 Unsteady flow interactions between an advected cylindrical vortex tube and a spherical particle. *J. Fluid Mech.* **288**, 123–155.

KIM, I., ELGHOBASHI, S. & SIRIGNANO, W.A. 1997 Unsteady flow interactions between a pair of advected vortex tubes and a rigid sphere. *Intl J. Multiphase Flow* **23** (1), 1–23.

LAMB, H. 1993 *Hydrodynamics*. Cambridge University Press.

LAW, C.K. 1976 Multicomponent droplet combustion with rapid internal mixing. *Combust. Flame* **26**, 219–233.

LAW, C.K. 1982 Recent advances in droplet vaporization and combustion. *Prog. Energy Combust. Sci.* **8** (3), 171–201.

LAZARO, B.J. & LASHERAS, J.C. 1992 Particle dispersion in the developing free shear layer. Part 2. Forced flow. *J. Fluid Mech.* **235**, 179–221.

LI, M. & CHRISTOFIDES, P.D. 2009 Modeling and control of high-velocity oxygen-fuel (HVOF) thermal spray: a tutorial review. *J. Therm. Spray Technol.* **18** (5), 753–768.

MAJEE, S., SAHA, A., CHAUDHURI, S., CHAKRAVORTTY, D. & BASU, S. 2021 Two-dimensional mathematical framework for evaporation dynamics of respiratory droplets. *Phys. Fluids* **33** (10), 103302.

MARCU, B. & MEIBURG, E. 1996 Three-dimensional features of particle dispersion in a nominally plane mixing layer. *Phys. Fluids* **8** (9), 2266–2268.

MASOUDI, M. & SIRIGNANO, W.A. 2000 Collision of a vortex with a vaporizing droplet. *Intl J. Multiphase Flow* **26** (12), 1925–1949.

MELLOR, A.M. 1980 Semi-empirical correlations for gas turbine emissions, ignition, and flame stabilization. *Prog. Energy Combust. Sci.* **6** (4), 347–358.

MITTAL, R., NI, R. & SEO, J.-H. 2020 The flow physics of COVID-19. *J. Fluid Mech.* **894**.

NAYAR, K.G., PANCHANATHAN, D., MCKINLEY, G.H. & LIENHARD, J.H. 2014 Surface tension of seawater. *J. Phys. Chem. Ref. Data* **43** (4), 043103.

NG, C.S., CHONG, K.L., YANG, R., LI, M., VERZICCO, R. & LOHSE, D. 2021 Growth of respiratory droplets in cold and humid air. *Phys. Rev. Fluids* **6** (5), 054303.

NIAZMAND, H., SHAW, B.D., DWYER, H.A. & AHARON, I. 1994 Effects of Marangoni convection on transient droplet evaporation. *Combust. Sci. Technol.* **103** (1–6), 219–233.

ODAR, F. & HAMILTON, W.S. 1964 Forces on a sphere accelerating in a viscous fluid. *J. Fluid Mech.* **18** (2), 302–314.

OZTURK, A. & CETEGEN, B.M. 2004 Modeling of plasma assisted formation of precipitates in zirconium containing liquid precursor droplets. *Mater. Sci. Engng:* A **384** (1–2), 331–351.

PAWLOWSKI, L. 2009 Suspension and solution thermal spray coatings. *Surf. Coat. Technol.* **203** (19), 2807–2829.

PEACEMAN, D.W. & RACHFORD, H.H. JR. 1955 The numerical solution of parabolic and elliptic differential equations. *J. Soc. Ind. Appl. Maths* **3** (1), 28–41.

PERINI, F. & REITZ, R.D. 2016 Improved atomization, collision and sub-grid scale momentum coupling models for transient vaporizing engine sprays. *Intl J. Multiphase Flow* **79**, 107–123.

RENKSIZBULUT, M. & YUEN, M.C. 1983 Numerical study of droplet evaporation in a high-temperature stream. *Trans. ASME J. Heat Transfer* **105** (2), 389–397.

REVEILLON, J. & VERVISCH, L. 2005 Analysis of weakly turbulent dilute-spray flames and spray combustion regimes. *J. Fluid Mech.* **537**, 317–347.

ROSTI, M., CAVAIOLA, M., OLIVIERI, S., SEMINARA, A. & MAZZINO, A. 2021 Turbulence role in the fate of virus-containing droplets in violent expiratory events. *Phys. Rev. Res.* **3** (1), 013091.

RUEHL, C.R., CHUANG, P.Y. & NENES, A. 2008 How quickly do cloud droplets form on atmospheric particles? *Atmos. Chem. Phys.* **8** (4), 1043–1055.

SAHA, A., DEEPU, P. & BASU, S. 2018 Transport phenomena in functional droplets. In *Droplet and Spray Transport: Paradigms and Applications* (ed. S. Basu, A. Agarwal, A. Mukhopadhyay & C. Patel), pp. 55–81. Springer.

SAHA, A., KUMAR, R. & BASU, S. 2010 Infrared thermography and numerical study of vaporization characteristics of pure and blended bio-fuel droplets. *Intl J. Heat Mass Transfer* **53** (19–20), 3862–3873.

SAHA, A., MAJEE, S., CHAUDHURI, S. & BASU, S. 2022 Evaporation and precipitation dynamics of a respiratory droplet. In *Drying of Complex Fluid Drops* (ed. D. Brutin & K. Sefiane), pp. 191–214. The Royal Society of Chemistry.

SAHA, A., SEAL, S., CETEGEN, B., JORDAN, E., OZTURK, A. & BASU, S. 2009*a* Thermo-physical processes in cerium nitrate precursor droplets injected into high temperature plasma. *Surf. Coat. Technol.* **203** (15), 2081–2091.

SAHA, A., SINGH, V., SEAL, S. & BASU, S. 2009*b* Vaporization and precipitation characteristics of cerium nitrate precursor droplets heated by monochromatic irradiation. *Surf. Coat. Technol.* **203** (15), 2102–2115.

SAZHIN, S.S. 2006 Advanced models of fuel droplet heating and evaporation. *Prog. Energy Combust. Sci.* **32** (2), 162–214.

SAZHIN, S.S. 2017 Modelling of fuel droplet heating and evaporation: recent results and unsolved problems. *Fuel* **196**, 69–101.

SENDA, J., HIGAKI, T., SAGANE, Y., FUJIMOTO, H., TAKAGI, Y. & ADACHI, M. 2000 Modeling and measurement on evaporation process of multicomponent fuels. *SAE Trans.* **109**, 347–358.

SHARMA, S., JAIN, S., SAHA, A. & BASU, S. 2022 Evaporation dynamics of a surrogate respiratory droplet in a vortical environment. *J. Colloid Interface Sci.* **623**, 541–551.

SHARMA, S., SINGH, A.P. & BASU, S. 2021 On the dynamics of vortex–droplet co-axial interaction: insights into droplet and vortex dynamics. *J. Fluid Mech.* **918**.

SHAW, R.A. 2003 Particle-turbulence interactions in atmospheric clouds. *Annu. Rev. Fluid Mech.* **35** (1), 183–227.

SHAW, R.A., READE, W.C., COLLINS, L.R. & VERLINDE, J. 1998 Preferential concentration of cloud droplets by turbulence: effects on the early evolution of cumulus cloud droplet spectra. *J. Atmos. Sci.* **55** (11), 1965–1976.

SIRIGNANO, W.A. 1983 Fuel droplet vaporization and spray combustion theory. *Prog. Energy Combust. Sci.* **9** (4), 291–322.

SIRIGNANO, W.A. 2010 *Fluid Dynamics and Transport of Droplets And Sprays*. Cambridge University Press.

SOMSEN, G.A., VAN RIJN, C., KOOIJ, S., BEM, R.A. & BONN, D. 2020 Small droplet aerosols in poorly ventilated spaces and SARS-CoV-2 transmission. *Lancet Respir. Med.* **8** (7), 658–659.

TANG, L.F., WEN, F., YANG, Y., CROWE, C.T., CHUNG, J.N. & TROUTT, T.R. 1992 Self-organizing particle dispersion mechanism in a plane wake. *Phys. Fluids* A **4** (10), 2244–2251.

VAILLANCOURT, P.A. & YAU, M.K. 2000 Review of particle-turbulence interactions and consequences for cloud physics. *Bull. Am. Meteorol. Soc.* **81** (2), 285–298.

VAN WYLEN, G.J. & SONNTAG, R.E. 1978 *Fundamentals of Classical Thermodynamics*. Wiley & Sons.

VEJERANO, E.P. & MARR, L.C. 2018 Physico-chemical characteristics of evaporating respiratory fluid droplets. *J. R. Soc. Interface* **15** (139), 20170939.

WORLD HEALTH ORGANIZATION 2020 Modes of transmission of virus causing COVID-19: implications for ipc precaution recommendations: scientific brief, 29 march 2020. *Tech. Rep.* World Health Organization.